# Noncyclic nonadiabatic geometric quantum gates in a superconducting circuit

Zhuang Ma,[1,‡] Jianwen Xu,[1,‡] Tao Chen,[2,‡] Yu Zhang,[1] Wen Zheng,[1] Shaoxiong Li,[1] Dong Lan,[1,3] Zheng-Yuan Xue,[2,*] Xinsheng Tan,[1,3,†] and Yang Yu[1,3]

[1] *National Laboratory of Solid State Microstructures, School of Physics, Nanjing University, Nanjing 210093, China*

[2] *Guangdong Provincial Key Laboratory of Quantum Engineering and Quantum Materials, and School of Physics and Telecommunication Engineering, South China Normal University, Guangzhou 510006, China*

[3] *Hefei National Laboratory, Hefei 230088, China*

(Received 6 October 2022; revised 22 June 2023; accepted 23 October 2023; published 22 November 2023)

Quantum gates based on geometric phases possess intrinsic noise-resilience features and attract much attention. However, the implementations of previous geometric quantum computation typically require a long pulse time of gates. As a result, their experimental control inevitably suffers from the cumulative disturbances of systematic errors due to excessive time consumption. Here, we experimentally implement noncyclic and nonadiabatic geometric quantum gates in a superconducting circuit, significantly shortening the gate time. Moreover, we experimentally verify that our universal single-qubit geometric gates are more robust to both the Rabi frequency and the qubit frequency shift-induced error, compared with the conventional dynamical gates, using the randomized benchmarking method. This scheme can also be utilized to construct two-qubit geometric operations while the generation of maximally entangled Bell states is demonstrated. Therefore, our results provide a promising routine to achieve fast, high-fidelity, and error-resilient quantum gates in superconducting quantum circuits.

DOI: 10.1103/PhysRevApplied.20.054047

## I. INTRODUCTION

The superconducting quantum circuit is one of the promising candidates for future large-scale quantum computation [1] due to its high controllability and scalability. However, at this stage, the major obstacle is the relatively short coherence time and experimental perturbations, which demand a speeding up of quantum operations and improving the robustness against errors under experimental controls in superconducting quantum circuits. Therefore, with their intrinsic noise-resilience features, gates induced by geometric phases [2–4], attainable in superconducting systems, are highly anticipated.

Geometric phases depend only on the global properties of their evolution paths so that they can be applied to construct geometric quantum gates against certain local noises [5]. Adiabatic geometric quantum computation (AGQC) based on the Berry phase has been proposed [3,6–8] and experimentally demonstrated in nuclear magnetic resonance [4], aiming to realize high-fidelity and robust quantum gates. However, the long gate time due to the adiabatic and cyclic evolution conditions restricts the practical application of AGQC, especially in quantum systems with limited coherence time. Some approaches have been proposed to overcome this problem, including the shortcut acceleration to the adiabatic evolution [9–12], while these inevitably sacrifice some robustness and generally increase the control complexity. Recently, nonadiabatic geometric quantum computation (NGQC) has been theoretically proposed and experimentally implemented based on Abelian [13–21] and non-Abelian geometric phases [22–31]. However, to strictly satisfy the cyclic evolution in NGQC, it usually requires at least $\pi$-pulse time consumption to construct a geometric gate, so there is still no advantage in operation time compared with conventional dynamical gates. Meanwhile, the increase in time consumption will also be accompanied by cumulative disturbances from systematic errors, making the robust advantage of the geometric gate displays ambiguous in experiments.

Some theoretical schemes based on nonadiabatic but noncyclic geometric evolution have recently been proposed [32–34]. The aim is to reduce the gate-operation time and release the restriction of cyclicity in the design of geometric gates [35]. One such scheme has been experimentally implemented in a single trapped ultracold $^{40}Ca^{+}$ ion [36], in which a special single-qubit geometric gate has demonstrated its error-resilient feature. However, the experimental verification of short-time and error-resilient features for a set of universal geometric gates is still

*zyxue83@163.com
†tanxs@nju.edu.cn
‡These three authors contributed equally to this work.

 

lacking, especially for the simultaneous suppression of different types of errors.

Here, we experimentally implement noncyclic and nonadiabatic (NCNA) geometric quantum computation in a superconducting quantum circuit. The method we adopt to construct NCNA geometric gates is reverse engineering, which purposefully determines the Hamiltonian for the system to generate noncyclic geometric evolution paths [37]. In our experiment, a set of universal and short-time single-qubit NCNA geometric gates including [38] the $\pi/8$ ($T$) gate, phase ($S$) gate, and Hadamard ($H$) gate are realized. Their high fidelities are characterized via randomized benchmarking (RB). Remarkably, we also experimentally demonstrate the strong resistance of our universal single-qubit NCNA geometric gates to both the Rabi frequency error and the qubit frequency shift-induced error. Finally, we implement nontrivial two-qubit geometric operation using parametric modulation [39–41] to generate maximally entangled Bell states.

## II. THEORETICAL SCHEME OF NCNA

We briefly elucidate the theoretical proposal [37] of constructing NCNA geometric gates in a superconducting qubit. With $\hbar = 1$, a general Hamiltonian for a two-level system is

$$\mathcal{H}(t) = \frac{1}{2}\begin{pmatrix} -\Delta(t) & \Omega(t)e^{-i\phi(t)} \\ \Omega(t)e^{i\phi(t)} & \Delta(t) \end{pmatrix}, \tag{1}$$

where $\Omega(t)$ and $\phi(t)$ are the time-dependent amplitude and phase of the driving microwave field, respectively; $\Delta(t) = \omega_q - \omega_m$ is the time-dependent detuning between the qubit transition frequency and the frequency of a microwave field. According to the Lewis-Riesenfeld invariant methods [42–44], we can choose a set of orthogonal states as $|\psi_+(t)\rangle = e^{if_+(t)}[\cos(\chi(t)/2)|0\rangle + \sin(\chi(t)/2)e^{i\xi(t)}|1\rangle]$ and $|\psi_-(t)\rangle = e^{if_-(t)}[\sin(\chi(t)/2)e^{-i\xi(t)}|0\rangle - \cos(\chi(t)/2)|1\rangle]$, in which $f_+(t) = f_-(t) = \gamma$ is regarded as a global phase and $\chi(t)$ and $\xi(t)$ represent the polar and azimuthal angles on a Bloch sphere, respectively. The entire noncyclic evolution path composed of three path segments needs to be utilized, as denoted in Fig. 1(a). We here take the evolution details of state vector $|\psi_+(t)\rangle$ as an illustration: first, it evolves along the longitude line from the initial point $(\chi_1, \xi_1)$ to $(\chi_2, \xi_1)$ at time $t = \tau_1$, with a null accumulation of the global phase; next, the state evolves along the latitude line from $(\chi_2, \xi_1)$ to $(\chi_2, \xi_2)$ at time $t = \tau_2$; the third path is similar to the reverse of the first path, which is from $(\chi_2, \xi_2)$ to the final point $(\chi_1, \xi_2)$. Among them, after strictly eliminating the dynamical phase existing in the middle segment by setting $\int_{\tau_1}^{\tau_2}\Delta(t)dt = (\xi_1 - \xi_2)\sin^2\chi_2$,

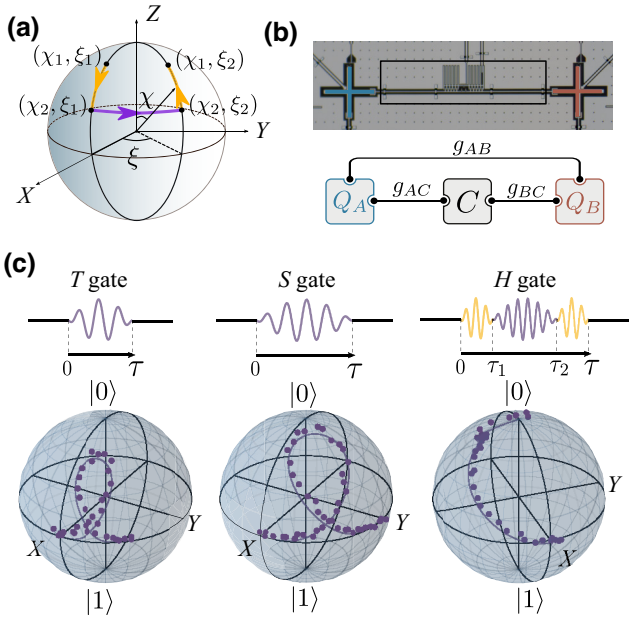


FIG. 1. Single-qubit NCNA geometric gates. (a) The noncyclic evolution path of state vector $|\psi_+(t)\rangle$ with Bloch representation to realize NCNA geometric gates. (b) Sketch of a two-qubit system with a coupler. $Q_A$ (blue) and $Q_B$ (red) are directly coupled with an effective coupling strength $g_{AB}$ and the coupling strength between the coupler $C$ (black) and $Q_A$ ($Q_B$) is $g_{AC}$ ($g_{BC}$). (c) The experimental pulses to realize NCNA geometric $T$, $S$, and $H$ gates and the corresponding evolution trajectories with specific initial states.

the accumulated geometric phase can be obtained as

$$\begin{aligned}\gamma_g &= -\frac{1}{2}\int_0^{\tau}\dot{\xi}(t)[1-\cos\chi(t)]dt \\ &= -\frac{1}{2}(\xi_2-\xi_1)(1-\cos\chi_2),\end{aligned} \tag{2}$$

which is exactly half of the solid angle enclosed by the noncyclic evolution path and its geodesic connecting the initial point $(\chi_1, \xi_1)$ and the final point $(\chi_1, \xi_2)$. Based on these, the corresponding Hamiltonian parameter $\phi(t)$ and the pulse area associated with $\Omega(t)$ can then be reverse-engineered in the three segments $t \in [0, \tau_1]$, $[\tau_1, \tau_2]$, and $[\tau_2, \tau]$ as

$$\begin{aligned}&\phi(t) = \xi_1 + \frac{\pi}{2}, \quad \frac{1}{2}\int_0^{\tau_1}\Omega(t)dt = \frac{1}{2}(\chi_2-\chi_1), \\ &\phi(t) = \xi(t) + \pi, \quad \frac{1}{2}\int_{\tau_1}^{\tau_2}\Omega(t)dt = \frac{1}{4}(\xi_2-\xi_1)\sin(2\chi_2), \\ &\phi(t) = \xi_2 - \frac{\pi}{2}, \quad \frac{1}{2}\int_{\tau_2}^{\tau}\Omega(t)dt = \frac{1}{2}(\chi_2-\chi_1),\end{aligned} \tag{3}$$

TABLE I. Device parameters.

| Parameters | $Q_A$ | $Q_B$ | Coupler |
|---|---|---|---|
| Readout frequency (GHz) | 6.9506 | 7.0039 | 7.3240 |
| Qubit frequency (GHz) (sweet spot) | 5.9206 | 5.9016 | 8.7510 |
| Qubit frequency (GHz) (operating spot) | 5.7421 | 5.9016 | 6.8770 |
| Anharmonicity (MHz) | −257.9 | −258.9 | −204.6 |
| $T_1$ (μs) (sweet spot) | 11.24 | 10.42 | 2.16 |
| $T_2^*$ (μs) (sweet spot) | 13.28 | 12.99 | 4.60 |
| $T_1$ (μs) (operating spot) | 14.81 | 10.42 | |
| $T_2^*$ (μs) (operating spot) | 1.47 | 12.99 | |

TABLE II. Coupling parameters.

| Parameters | Coupling strength (MHz) |
|---|---|
| Qubit-coupler coupling strength $g_{AC}$ | 107 |
| Qubit-coupler coupling strength $g_{BC}$ | 89 |
| Qubit-qubit coupling strength $g_{AB}$ | 4.65 |

with detuning $\Delta(t) = 0,\ -(\xi_2 - \xi_1)\sin^2\chi_2/(\tau_2 - \tau_1)$, 0, where $\xi(t) = \xi_1 - \int_{\tau_1}^{t} \Delta(t')\,dt' + \cot\chi_2 \int_{\tau_1}^{t} \Omega(t')\,dt'$. In this way, the resulting evolution operator is given by

$$U(\tau) = \begin{pmatrix} (c_{\gamma'} + is_{\gamma'}c_{\chi_1})e^{-i\xi_-} & is_{\gamma'}s_{\chi_1}e^{-i\xi_+} \\ is_{\gamma'}s_{\chi_1}e^{i\xi_+} & (c_{\gamma'} - is_{\gamma'}c_{\chi_1})e^{i\xi_-} \end{pmatrix}, \tag{4}$$

where $c_j = \cos j$, $s_j = \sin j$, $\xi_\pm = [\xi_2 \pm \xi_1]/2$, and $\gamma' = \gamma_g + \xi_-$. We find that arbitrary NCNA geometric gates can be realized by setting parameters $\chi_1$, $\xi_{1,2}$, and $\gamma'$.

## III. QUBIT GEOMETRIC GATES

### A. Fabrication

Our experiment of the above NCNA geometric scheme is performed in a superconducting quantum circuit containing four tunable grounded transmon qubits, and four tunable floating couplers with cross-shaped capacitors [45]. Only two qubits $Q_A$ and $Q_B$ with a coupler $C$ are used in this experiment, with a sketch of the coupler system shown in Fig. 1(b). The procedures of fabrication and diagram of the measurement setup are the same as in Ref. [57], and a false-colored optical micrograph of the superconducting circuits and the corresponding circuit diagram are shown in Fig. 3. The parameter details of the sample we used in our experiment are shown in Table I and the parameters of the coupling strength are shown in Table II.

### B. Single-qubit gates

We first perform a set of universal single-qubit geometric gates, including the $T$, $S$, and $H$ gates at the sweet spot of $Q_A$ to demonstrate their high fidelities and error-resilient features. The envelope of each pulse is a truncated Gaussian pulse with DRAG (Derivative Reduction by Adiabatic Gate) procedure [46–48] to suppress the leakage error. To realize NCNA geometric $T$ and $S$ gates, the parameters in Eq. (3) are set as $\xi_2 - \xi_1 = 9\pi/4$ and $5\pi/2$, respectively, with the same $\gamma' = \pi$, where we choose $\chi_1 = \chi_2$ to ensure that the operation time consumed is the shortest. In addition, for the NCNA geometric $H$ gate, we set $\chi_1 = \pi/2$, $\gamma' = \pi/4$, and $\xi_2 - \xi_1 = (2n+1)\pi$, where $\xi_1 = \pi/2$ and $n$ is an integer. To optimize the total pulse area, which corresponds to $n$, we determine $n = 0$ in practice, with the limitation of sampling rate and output voltage of arbitrary waveform generators. Using these NCNA geometric gates obtained, we implement the geometric evolution control for the special initial states, and their corresponding evolution trajectories are shown in Fig. 1(c).

In this case, the pulse areas $\frac{1}{2}\int_0^\tau \Omega(t)dt$ for these NCNA geometric $T$, $S$, and $H$ gates are about $0.46\pi$, $0.60\pi$, and $0.38\pi$, which can be solved by substituting the gate parameters into Eq. (3). It can be confirmed that our noncyclic and nonadiabatic geometric gates have the advantage of shorter gate time compared with the single-loop geometric scheme [20] and the conventional dynamical scheme (see Appendix A or Ref. [37] for details). On the other hand, compared with the single-loop geometric evolution path [20], our noncyclic geometric evolution path in Fig. 1(a) is shorter because it does not need to pass strictly through the north and south poles of the Bloch sphere.

Due to the smaller pulse area involved, the NCNA geometric scheme has an advantage in operating time compared with the conventional dynamical and single-loop geometric gate [20], enabling higher gate fidelity and inheriting geometric error-resilient features. In this article, both advantages are characterized via Clifford-based RB [51–53]. The experimental sequences of the reference RB and interleaved RB are shown in the inset of Fig. 2. From the reference and interleaved RB, we obtain the depolarizing parameters $p_{\mathrm{ref}}$ and $p_{\mathrm{itl}}$ by fitting the experimental results shown in Fig. 2, with $F = Ap^m + B$. Here $A$ and $B$ are constants that absorb preparation and measurement errors and $m$ is the number of Clifford gates. For the single-qubit gate, the reference gate fidelity is $F_{\mathrm{ref}} = 1 - (1 - p_{\mathrm{ref}})(d-1)/d/1.875 = 0.9943$ with $d = 2$ and the fidelities $F_{\mathrm{itl}} = 1 - (1 - p_{\mathrm{itl}}/p_{\mathrm{ref}})(d-1)/d$ of interleaved $2T$, $S$, and $H$ gates are 0.9982, 0.9995, and 0.9994, respectively (since the $T$ gate is not a Clifford generator, we apply two $T$ gates in series to demonstrate the fidelity of the NCNA geometric $T$ gate [54]).

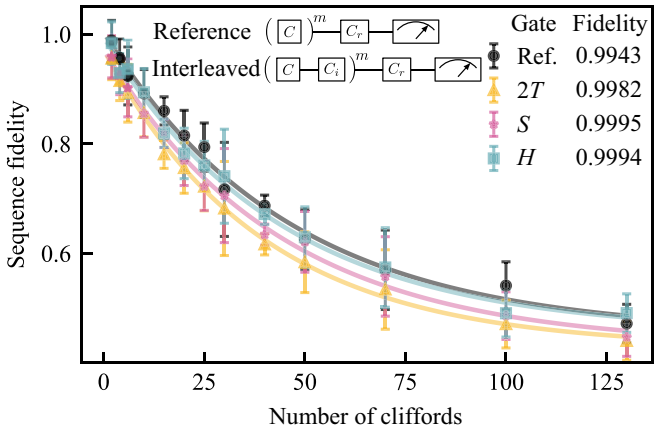


FIG. 2. Clifford-based RB of single-qubit NCNA geometric gates. The inset is the sequence of gates from the Clifford group for the reference RB and interleaved RB. Sequence fidelities are functions of the number of Cliffords, and the exponential decay curves give fidelities of NCNA gates: the $2T$, $S$, and $H$ gates.

### C. Robustness of the geometric scheme

Furthermore, to verify the gate robustness of the NCNA geometric scheme, we next consider the error-affected Hamiltonian as follows:

$$\mathcal{H}(t) = \frac{1}{2}\begin{pmatrix} -(\Delta+\delta\Omega_m) & (1+\epsilon)\Omega(t)e^{-i\phi(t)} \\ (1+\epsilon)\Omega(t)e^{i\phi(t)} & (\Delta+\delta\Omega_m) \end{pmatrix}, \tag{5}$$

where $\epsilon$ and $\delta$ represent the pulse amplitude (Rabi frequency) error and the qubit frequency shift-induced error, respectively, and $\Omega_m$ is the maximum of $\Omega(t)$. In the experiment, these errors are generated by the designed microwave pulses. We continue to compare the robustness of the error-affected NCNA geometric $2T$, $S$, and $H$ gates with the corresponding dynamical counterparts using interleaved RB. To numerically simulate the RB results, we compute all propagators of the system Hamiltonian, considering the relaxation and dephasing time. We also consider the second excited state to calculate the population leakage. Similar to the experimental RB procedure, the propagators are applied to the state density matrix in the vector representation. Then the fidelities of numerical simulation can be finally obtained. As shown in Fig. 4, our experimental and numerical results demonstrate the suppression effects of NCNA geometric $2T$, $S$, and $H$ gates on both the Rabi frequency error and the qubit frequency shifted-induced error. Thus, we experimentally implement a set of universal single-qubit NCNA geometric gates, which outperform dynamical gates comprehensively in gate robustness and gate time.

## IV. ENTANGLED STATES GENERATED BY GEOMETRIC MANIPULATIONS

The implementation of quantum computation also involves entangled interactions between qubits. In this article, we experimentally demonstrate that the NCNA geometric scheme can also be applied to two-qubit manipulations by using parametric modulation [39–41]. The coupling model in our experiment consisting of two qubits $Q_{A,B}$ and a coupler $C$ is shown in Fig. 1(b). $Q_A$ and $Q_B$ are biased at the operating spot and the sweet spot, respectively, and the coupler $C$ is modulated using a parametric pulse in the form of $\phi(t) = \phi_{\rm dc} + \epsilon_p \cos(\omega_p t + \phi_p)$, in which $\phi_{\rm dc}$, $\epsilon_p$, $\omega_p$, and $\phi_p$ are the dc flux bias, modulation amplitude, frequency, and phase, respectively. After neglecting the high-order oscillating terms and applying the unitary transformation, the final effective Hamiltonian

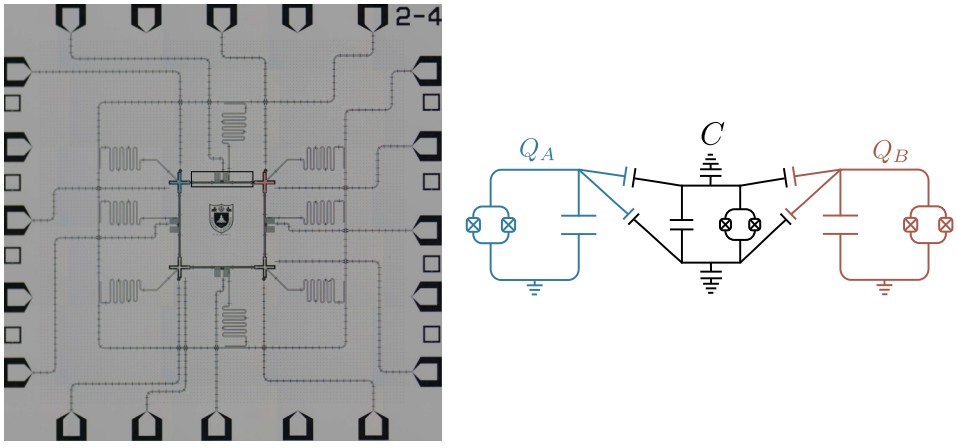


FIG. 3. Left panel: False-colored optical micrograph of the superconducting circuits, including four tunable grounded transmon qubits and four tunable floating couplers. $Q_A$ (blue), $Q_B$ (red), and the coupler $C$ (black) in the middle of two qubits are chosen in this experiment. Right panel: Circuit diagram of two qubits and the coupler.

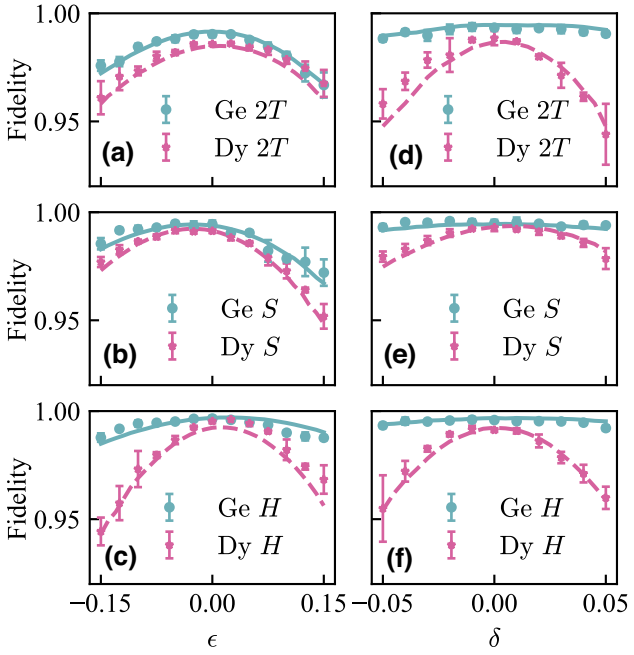


FIG. 4. Error-resilient feature of NCNA geometric gates. (a)–(c) The experimental sequence fidelities as functions of the Rabi frequency error $\epsilon$ with the interleaved RB of single-qubit geometric and dynamical gates: (a) $2T$, (b) $S$, and (c) $H$ are realized. (d)–(f) The experimental sequence fidelities as functions of the qubit frequency shift-induced error $\delta$ with the interleaved RB of single-qubit gates: (d) $2T$, (e) $S$, and (f) $H$ are realized. The experimental results are consistent with the numerical simulation results using QuTiP [49,50], and the teal solid line and fuchsia dashed line represent the numerical simulation of geometric and dynamical gates, respectively.

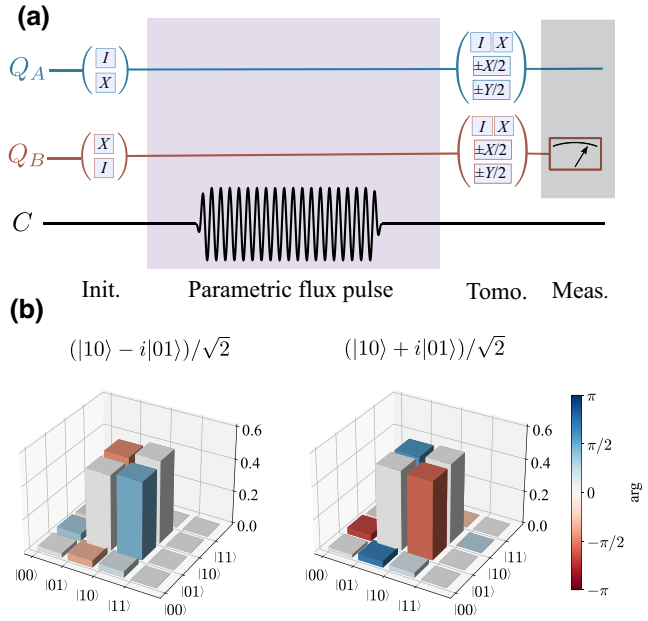


FIG. 5. Bell states generated by the two-qubit NCNA geometric manipulation. (a) The whole pulse sequence is used to demonstrate the Bell states. The system can be initialized in $|01\rangle$ or $|10\rangle$, and then we perform a well-designed parametric flux pulse. Finally, we use single-qubit gates $I, X, \pm X/2$, and $\pm Y/2$ to implement a joint dispersive readout using the resonator of $Q_B$. (b) The density matrix of Bell states $(|10\rangle - i|01\rangle)/\sqrt{2}$ and $(|10\rangle + i|01\rangle)/\sqrt{2}$ generated by the two-qubit NCNA geometric operation. The heights and colors of bars in the histogram represent the corresponding amplitudes and arguments of density matrix elements.

within the subspace $\{|01\rangle, |10\rangle\}$ can be written as

$$H_{\text{eff}} = \frac{1}{2}\begin{pmatrix} -\Delta' & g_{\text{eff}} e^{-i(\eta t+\varphi)} \\ g_{\text{eff}} e^{i(\eta t+\varphi)} & \Delta' \end{pmatrix}, \tag{6}$$

where $g_{\text{eff}}$ and $\eta t + \varphi$ are the effective coupling strength and the time-dependent phase generated by modulation pulses, a detailed derivation of which can be found in Appendix B, while the detuning $\Delta'$ is defined as $\omega_p - (\omega_{01} - \omega_{10})$.

Noticing that the above Hamiltonian is similar to that of a single-qubit one $\mathcal{H}(t)$, we can design the parameters to implement arbitrary entangled two-qubit geometric manipulation in the subspace spanned by $\{|01\rangle, |10\rangle\}$, and the experimental pulse sequence is shown in Fig. 5(a). The unitary operator is written as

$$U = \begin{pmatrix} 1 & 0 & 0 & 0 \\ 0 & \cos\left(\frac{\vartheta}{2}\right) & i\sin\left(\frac{\vartheta}{2}\right) e^{i\beta} & 0 \\ 0 & i\sin\left(\frac{\vartheta}{2}\right) e^{-i\beta} & \cos\left(\frac{\vartheta}{2}\right) & 0 \\ 0 & 0 & 0 & 1 \end{pmatrix}, \tag{7}$$

where $\vartheta$ and $\beta$ are the rotation angles. However, the geometric $i$SWAP gate via parametric modulation needs multiple tiny segments of the geometric path, which is not well realized due to the performance of the instruments. Without loss of generality, we demonstrate our scheme by preparing high-fidelity entangled Bell states.

In practice, we set $\chi_1 = \chi_2 = 0.789$ and $\xi_2 - \xi_1 = 3\pi/2$. The modulation phase $\phi_p = \pi$ and the amplitude $\epsilon_p$ are designed to induce the effective strength $g_{\text{eff}} = 3.96$ MHz. The frequency of modulation pulse becomes $\omega_p = \omega_{01} - \omega_{10} + g_{\text{eff}} \cot \chi_2 = 163.7$ MHz. To generate high-fidelity Bell states, the duration of the longitudinal waveform is calibrated through the population in the subspace $\{|01\rangle, |10\rangle\}$ (see Appendix B for details). We carefully design the pulse area with the width of the rising, square, and falling pulses being 10, 78, and 10 ns, respectively. Here, we perform two-qubit state tomography using a joint dispersive readout [55,56] to detect Bell states shown in Fig. 5(b). The two-qubit system is initialized in the state $|10\rangle$ ($|01\rangle$) and then the pulse of the entangled operation is applied to the flux of the coupler $C$. The Bell

states can be reconstructed by implementing an overcomplete raw measurement involving different combinations of single-qubit gates $I$, $X$, $\pm X/2$, and $\pm Y/2$ on $Q_A$ ($Q_B$) (see Appendix C for details). The generated Bell states are $(|10\rangle - i|01\rangle)/\sqrt{2}$ and $(|10\rangle + i|01\rangle)/\sqrt{2}$ with fidelities 97.89% and 98.07% when the corresponding initial states are $|10\rangle$ and $|01\rangle$. The comparisons of experimental and ideal Bell states are shown in Appendix C.

## V. CONCLUSION

In summary, we experimentally implement short-time and high-fidelity NCNA geometric gates in a superconducting circuit and demonstrate that these gates are more robust to both the Rabi frequency error and the qubit frequency shift-induced error compared with the conventional dynamical gates. In addition, the approach can be generalized to two-qubit manipulation to generate Bell states. Therefore, the NCNA geometric gates are promising candidates for fast, high-fidelity, and robust universal quantum operations.

## ACKNOWLEDGMENTS

This work is partly supported by the Key R&D Program of Guangdong Province (Grant No. 2018B030326001), NSFC (Grants No. 12074179, No. 11890704, No. U21A20436, and No. 12305019), NSF of Jiangsu Province (Grant No. BE2021015-1), and Innovation Program for Quantum Science and Technology (2021ZD0301702).

## APPENDIX A: DYNAMICAL QUANTUM GATES

The construction of universal dynamical single gates, mentioned in our main text, needs to be based on a resonant two-level drive. The corresponding Hamiltonian is the same as Eq. (1) with $\Delta(t) = 0$, where the driving phase $\phi(t) = \phi_d$ is a constant to ensure that there is no accumulation of geometric phase, i.e., $\gamma_g = 0$. In this way, the dynamical $\pi/8$ ($T$), phase ($S$), and Hadamard ($H$) gates are respectively obtained by the operations of $R_y(-\pi/2)R_x(\pi/4)R_y(\pi/2)$, $R_y(-\pi/2)R_x(\pi/2)R_y(\pi/2)$, and $R_x(\pi)R_y(\pi/2)$, where operation elements $R_x(\theta)$ and $R_y(\theta)$ are the dynamical $X$-axis and $Y$-axis rotation operations for arbitrary angle $\theta = \int_0^\tau \Omega(t)dt$, which can be done by determining $\phi_d = 0$ and $\pi/2$, respectively. The calculation results show that the pulse areas required to construct dynamical $T$, $S$, and $H$ gates are $0.625\pi$, $0.75\pi$, and $0.75\pi$, respectively. For fair comparison, the pulse envelope of each dynamical gate is the same as the corresponding geometric gate with DRAG procedure.

## APPENDIX B: TWO-QUBIT GEOMETRIC GATE

With the restriction of the noncyclic geometric path, the pure geometric phase cannot be completely satisfied in the realization of the noncyclic geometric control-Z (CZ) gate that depends on the extra geometric parameter space. So, we utilize the NCNA protocol to generate a two-qubit NCNA geometric gate in the subspace $\{|01\rangle, |10\rangle\}$. The realization of our geometric $i$SWAP gate also requires a three-segment geometric evolution path, where the first and third segments are very short with the pulse area being $\int_0^{\tau_1} g_{\text{eff}}dt = \int_{\tau_2}^{\tau_3} g_{\text{eff}}dt = \pi/2 - \arccos(1/3) \approx \pi/9$. For the two-qubit operation via parametric modulation, the pulse area is too small to calibrate the pulse duration, because of the nonlinear effects due to hardware constraints when dealing with the short pulses and nonlinear relationships in tunable coupler schemes [58]. In the experiment via parametric modulation, we usually use the rising edge lower than the modulation frequency to suppress the phase difference between microwave and flux pulses [59]. In our proposal, those segments require the rising edge and the falling edge resulting in longer gate durations. Furthermore, the first and third segments of the whole flux pulse are resonant while the second is near-resonant to satisfy our theoretical condition, where the phase correction is intractable. The final fidelity of our experimental data is limited by the performance of our experimental equipment including sampling rates and amplitudes. If there were to be more advanced equipment, the advantages of this scheme will be better demonstrated.

In this article, we demonstrate the generation of Bell states without loss of generality, while only the second separate is required in the whole noncyclic geometric path. The corresponding evolution operator is

$$U(\tau_2, \tau_1) = \begin{pmatrix} e^{-i\frac{\xi_2-\xi_1}{2}} & 0 \\ 0 & e^{i\frac{\xi_2-\xi_1}{2}} \end{pmatrix} \begin{pmatrix} \cos\gamma' + i\sin\gamma'\cos\chi_2 & i\sin\gamma'\sin\chi_2 e^{-i\xi_1} \\ i\sin\gamma'\sin\chi_2 e^{i\xi_1} & \cos\gamma' - i\sin\gamma'\cos\chi_2 \end{pmatrix}, \tag{B1}$$

where $\gamma' = \frac{1}{2}(\xi_2 - \xi_1)\cos\chi_2$. To generate high-fidelity Bell states, the parameter should be set $\xi_2 - \xi_1 = n\pi/2$, $(n = 1, 2, 3, \ldots)$ and then we solve numerically $\chi_1 = \chi_2 = 0.78935$ when $\xi_2 - \xi_1 = 3\pi/2$ by applying the evolution operator to the initial state. The Hamiltonian parameters can be obtained by reverse-engineering, similar to the single-qubit NCNA scheme.

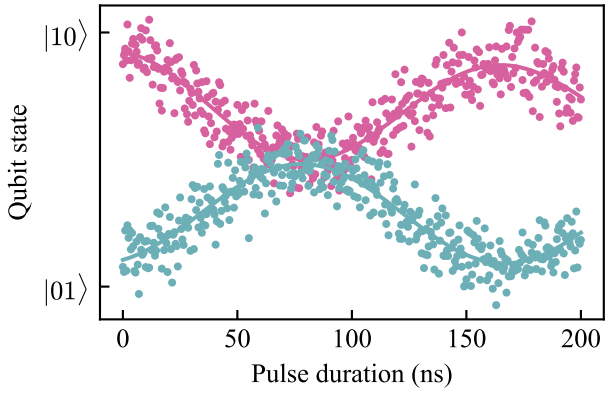


FIG. 6. Calibration of the Bell states. The fuchsia and teal points are experimental populations in the subspace $\{|01\rangle, |10\rangle\}$, and the corresponding solid lines are fitted curves.

By applying a parametric pulse $\phi(t) = \phi_{\rm dc} + \epsilon_p \cos(\omega_p t + \phi_p)$, where $\phi_{\rm dc}$, $\epsilon_p$, $\omega_p$, and $\phi_p$ are the dc flux bias, modulation amplitude, frequency, and phase, respectively, then we can obtain the effective Hamiltonian in the space spanned by $\{|01\rangle, |10\rangle\}$, which is written as

$$H_{\rm eff} = \frac{\epsilon_p}{2}\frac{\partial J_{AB}}{\partial \phi}|01\rangle\langle 10|e^{i(\Delta_t t+\phi_p)} + \text{H.c.} \qquad \text{(B2)}$$

Here $\Delta_t = \omega_p - (\omega_B - \omega_A)$, with $\Delta_t \ll \{(\omega_B - \omega_A), \omega_p\}$, and $J_{AB} = g_{AB} + (g_{AC}g_{BC}/\Delta(\phi))$, where $\Delta(\phi) = 2/\{[1/(\omega_A - \omega_C)] + [1/(\omega_B - \omega_C)]\}$. To calibrate the parametric modulation is the first step for this Bell state generation. The dc flux bias, modulation amplitude, and phase are fixed as $\phi_{\rm dc} = -0.26\Phi_0$, $\epsilon_p = 0.03\Phi_0$, and $\phi_p = 0$ in the calibration. By sweeping the parametric frequency, the parametric modulation is calibrated to obtain the resonant frequency $\omega_p^r = 159.8$ MHz and the effective coupling $g_{\rm eff} = 3.96$ MHz.

Applying unitary transformation $V(t) = e^{-i\Delta'/2(|01\rangle\langle 01| - |10\rangle\langle 10|)t}$, we can rewrite the above equation as

$$H_{\rm eff} = \frac{1}{2}\begin{pmatrix} -\Delta' & g_{\rm eff}e^{-i(\eta t+\varphi)} \\ g_{\rm eff}e^{i(\eta t+\varphi)} & \Delta' \end{pmatrix}, \qquad \text{(B3)}$$

where $g_{\rm eff} = \epsilon_p \partial J_{AB}/\partial\phi$, $\Delta' = \Delta_t - \eta$, $\varphi = \text{const.}$, and $\eta$ represents a tunable parameter. Here, the parameters of the Hamiltonian [similar to a general Hamiltonian for a two-level system, Eq. (1)] and the parametric pulse can then be reverse-engineered according to the second segment of the evolution path combining with the known values of $\chi_2$, $\xi_1$, $\xi_2$, and $g_{\rm eff}$, i.e., $\Delta_t = g_{\rm eff}\cot\chi_2$ and $\phi_p = \varphi = \pi$. So we have obtained all the values of the experimental parametric pulse: $\phi_{\rm dc} = -0.26\Phi_0$, $\epsilon_p = 0.03\Phi_0$, $\omega_p = \omega_p^r + g_{\rm eff}\cot\chi_2 = 163.7$ MHz, and $\phi_p = \pi$.

According to the features of parametric modulation, the evolution time should be precalibrated precisely. We first prepare $|10\rangle$ and $|01\rangle$, then apply a variable-length flux-modulation pulse to the coupler $C$ with $\omega_{p2} = 163.7$ MHz. The cross (at 78 ns) of two fitted population oscillation curves represents the evolution duration of the generated Bell states as shown in Fig. 6.

## APPENDIX C: BELL STATE TOMOGRAPHY USING A JOINT DISPERSIVE READOUT

Bell state tomography is performed following Ref. [55, 56], but here using an overcomplete set of 36 raw measurements. The raw measurements consist of rotations chosen from $\{I, R_x^{+\pi}, R_x^{+\pi/2}, R_y^{+\pi/2}, R_x^{-\pi/2}, R_y^{-\pi/2}\}$, which are applied to two qubits $Q_A$ and $Q_B$ simultaneously. The

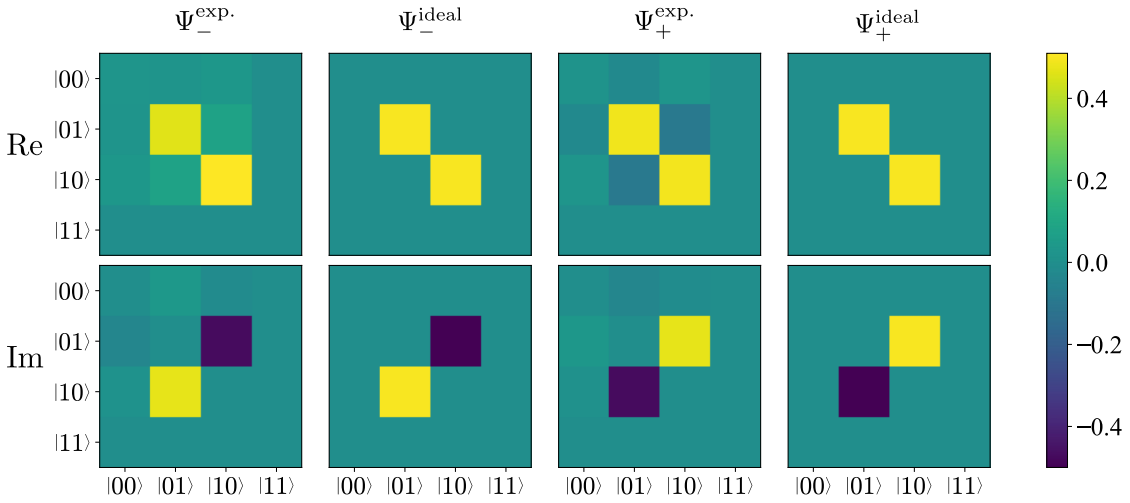


FIG. 7. Comparison of experimental and ideal Bell state tomography. The upper and lower diagrams represent real parts and imaginary parts of these Bell states $\Psi_\pm = (|10\rangle \pm i|01\rangle)/\sqrt{2}$.

ensemble averages of raw measurements are obtained by repeating them 250 000 times.

To retain the Hermiticity and positivity properties of state density matrices, maximum likelihood estimation (MLE) is applied. The Hermitian and positive-semidefinite density matrix $\rho$ can be parameterized as

$$\rho = \frac{T^\dagger T}{\mathrm{tr}\left(T^\dagger T\right)} \tag{C1}$$

using the Cholesky decomposition, where

$$T = \begin{pmatrix} t_1 & 0 & 0 & 0 \\ t_5 + it_6 & t_2 & 0 & 0 \\ t_{11} + it_{12} & t_7 + it_8 & t_3 & 0 \\ t_{15} + it_{16} & t_{13} + it_{14} & t_9 + it_{10} & t_4 \end{pmatrix} \tag{C2}$$

is a lower triangular matrix and $t_i$ are the optimized parameters by MLE. According to the results of 36 raw measurements, the guessed density matrix $\rho_0$ can be obtained by solving the linear system of equations. And then the likelihood function

$$\mathcal{L} = \sum_{i=1}^{36} \alpha_i \left(m_i - \mathrm{tr}\left(M_i \rho\right)\right)^2 \tag{C3}$$

is optimized to a minimum to obtain parameters $t_i$, where $\alpha_i$, $m_i$, and $M_i$ are weight factors, results of raw measurements, and measurement operators, respectively.

The experimental Bell state tomography using a joint dispersive readout is shown in Fig. 7, compared with the ideal Bell states[60].


[1] M. Kjaergaard, M. E. Schwartz, J. Braumuller, P. Krantz, J. I.-J. Wang, S. Gustavsson, and W. D. Oliver, Superconducting qubits: Current state of play, Annu. Rev. Condens. Matter Phys. **11**, 369 (2020).

[2] B. M. Victor, Quantal phase factors accompanying adiabatic changes, Proc. R. Soc. Lond. A **392**, 45 (1984).

[3] P. Zanardi and M. Rasetti, Holonomic quantum computation, Phys. Lett. A **264**, 94 (1999).

[4] J. A. Jones, V. Vedral, A. Ekert, and G. Castagnoli, Geometric quantum computation using nuclear magnetic resonance, Nature **403**, 869 (2000).

[5] S. L. Zhu and P. Zanardi, Geometric quantum gates that are robust against stochastic control errors, Phys. Rev. A **72**, 020301(R) (2005).

[6] J. Pachos, P. Zanardi, and M. Rasetti, Non-Abelian Berry connections for quantum computation, Phys. Rev. A **61**, 010305(R) (1999).

[7] A. Ekert, M. Ericsson, P. Hayden, H. Inamori, J. A. Jones, D. K. L. Oi, and V. Vedral, Geometric quantum computation, J. Mod. Opt. **47**, 2501 (2000).

[8] L.-M. Duan, J. I. Cirac, and P. Zoller, Geometric manipulation of trapped ions for quantum computation, Science **292**, 1695 (2001).

[9] M. Demirplak and S. Rice, Adiabatic population transfer with control fields, J. Phys. A: Math. Theor. **107**, 9937 (2003).

[10] M. V. Berry, Transitionless quantum driving, J. Phys. A Math. Theor. **42**, 365303 (2009).

[11] J. G. Muga, X. Chen, S. Ibáñez, I. Lizuain, and A. Ruschhaupt, Transitionless quantum drivings for the harmonic oscillator, J. Phys. B: At., Mol. Opt. Phys. **43**, 085509 (2010).

[12] S. Masuda and K. Nakamura, Fast-forward of adiabatic dynamics in quantum mechanics, Proc. R. Soc. Lond. A **466**, 1135 (2010).

[13] W. Xiang-Bin and M. Keiji, Nonadiabatic conditional geometric phase shift with NMR, Phys. Rev. Lett. **87**, 097901 (2001).

[14] S. L. Zhu and Z. D. Wang, Implementation of universal quantum gates based on nonadiabatic geometric phases, Phys. Rev. Lett. **89**, 097902 (2002).

[15] D. Leibfried, B. DeMarco, V. Meyer, D. Lucas, M. Barrett, J. Britton, W. M. Itano, B. Jelenković, C. Langer, T. Rosenband, and D. J. Wineland, Experimental demonstration of a robust, high-fidelity geometric two ion-qubit phase gate, Nature **422**, 412 (2003).

[16] S. L. Zhu and Z. D. Wang, Unconventional geometric quantum computation, Phys. Rev. Lett. **91**, 187902 (2003).

[17] J. Du, P. Zou, and Z. D. Wang, Experimental implementation of high-fidelity unconventional geometric quantum gates using an NMR interferometer, Phys. Rev. A **74**, 020302(R) (2006).

[18] P. Z. Zhao, X.-D. Cui, G. F. Xu, E. Sjoqvist, and D. M. Tong, Rydberg-atom-based scheme of nonadiabatic geometric quantum computation, Phys. Rev. A **96**, 052316 (2017).

[19] T. Chen and Z.-Y. Xue, Nonadiabatic geometric quantum computation with parametrically tunable coupling, Phys. Rev. Appl. **10**, 054051 (2018).

[20] Y. Xu, Z. Hua, T. Chen, X. Pan, X. Li, J. Han, W. Cai, Y. Ma, H. Wang, Y. P. Song, Z.-Y. Xue, and L. Sun, Experimental implementation of universal nonadiabatic geometric quantum gates in a superconducting circuit, Phys. Rev. Lett. **124**, 230503 (2020).

[21] P. Zhao, Z. Dong, Z. Zhang, G. Guo, D. Tong, and Y. Yin, Experimental realization of nonadiabatic geometric gates with a superconducting Xmon qubit, Sci. China: Phys., Mech. Astron. **64**, 250632 (2021).

[22] E. Sjoqvist, D. M. Tong, L. M. Andersson, B. Hessmo, M. Johansson, and K. Singh, Non-adiabatic holonomic quantum computation, New J. Phys. **14**, 103035 (2012).

[23] G. F. Xu, J. Zhang, D. M. Tong, E. Sjoqvist, and L. C. Kwek, Nonadiabatic holonomic quantum computation in decoherence-free subspaces, Phys. Rev. Lett. **109**, 170501 (2012).

[24] A. A. Abdumalikov, J. M. Fink, K. Juliusson, M. Pechal, S. Berger, A. Wallraff, and S. Filipp, Experimental realization of non-Abelian non-adiabatic geometric gates, Nature **496**, 482 (2013).

[25] G. Feng, G. Xu, and G. Long, Experimental realization of nonadiabatic holonomic quantum computation, Phys. Rev. Lett. **110**, 190501 (2013).

[26] C. Zu, W.-B. Wang, L. He, W.-G. Zhang, C.-Y. Dai, F. Wang, and L.-M. Duan, Experimental realization of universal geometric quantum gates with solid-state spins, Nature **514**, 72 (2014).

[27] Y. Xu, W. Cai, Y. Ma, X. Mu, L. Hu, T. Chen, H. Wang, Y. P. Song, Z.-Y. Xue, Z.-q. Yin, and L. Sun, Single-loop realization of arbitrary nonadiabatic holonomic single-qubit quantum gates in a superconducting circuit, Phys. Rev. Lett. **121**, 110501 (2018).

[28] B.-J. Liu, X.-K. Song, Z.-Y. Xue, X. Wang, and M.-H. Yung, Plug-and-play approach to nonadiabatic geometric quantum gates, Phys. Rev. Lett. **123**, 100501 (2019).

[29] T. Yan, B.-J. Liu, K. Xu, C. Song, S. Liu, Z. Zhang, H. Deng, Z. Yan, H. Rong, K. Huang, M.-H. Yung, Y. Chen, and D. Yu, Experimental realization of nonadiabatic shortcut to non-Abelian geometric gates, Phys. Rev. Lett. **122**, 080501 (2019).

[30] Z. Zhu, T. Chen, X. Yang, J. Bian, Z.-Y. Xue, and X. Peng, Single-loop and composite-loop realization of nonadiabatic holonomic quantum gates in a decoherence-free subspace, Phys. Rev. Appl. **12**, 024024 (2019).

[31] Z. Han, Y. Dong, B. Liu, X. Yang, S. Song, L. Qiu, D. Li, J. Chu, W. Zheng, J. Xu, T. Huang, Z. Wang, X. Yu, X. Tan, D. Lan, M.-H. Yung, and Y. Yu, Experimental realization of universal time-optimal non-Abelian geometric gates, ArXiv:2004.10364 (2020).

[32] T. Chen and Z.-Y. Xue, High-fidelity and robust geometric quantum gates that outperform dynamical ones, Phys. Rev. Appl. **14**, 064009 (2020).

[33] B.-J. Liu, S.-L. Su, and M.-H. Yung, Nonadiabatic noncyclic geometric quantum computation in Rydberg atoms, Phys. Rev. Res. **2**, 043130 (2020).

[34] L.-N. Ji, C.-Y. Ding, T. Chen, and Z.-Y. Xue, Noncyclic geometric quantum gates with smooth paths via invariant-based shortcuts, Adv. Quantum Technol. **4**, 2100019 (2021).

[35] A. Friedenauer and E. Sjoqvist, Noncyclic geometric quantum computation, Phys. Rev. A **67**, 024303 (2003).

[36] J. W. Zhang, L.-L. Yan, J. C. Li, G. Y. Ding, J. T. Bu, L. Chen, S.-L. Su, F. Zhou, and M. Feng, Single-atom verification of the noise-resilient and fast characteristics of universal nonadiabatic noncyclic geometric quantum gates, Phys. Rev. Lett. **127**, 030502 (2021).

[37] T. Chen, Z.-Y. Xue, and Z. D. Wang, Error-tolerant geometric quantum control for logical qubits with minimal resources, Phys. Rev. Appl. **18**, 014062 (2022).

[38] M. A. Nielsen and I. L. Chuang, *Quantum Computation and Quantum Information* (Cambridge University Press, Cambridge, 2012).

[39] D. C. McKay, S. Filipp, A. Mezzacapo, E. Magesan, J. M. Chow, and J. M. Gambetta, Universal gate for fixed-frequency qubits via a tunable bus, Phys. Rev. Appl. **6**, 064007 (2016).

[40] M. Ganzhorn, G. Salis, D. J. Egger, A. Fuhrer, M. Mergenthaler, C. Muller, P. Muller, S. Paredes, M. Pechal, M. Werninghaus, and S. Filipp, Benchmarking the noise sensitivity of different parametric two-qubit gates in a single superconducting quantum computing platform, Phys. Rev. Res. **2**, 033447 (2020).

[41] X. Y. Han, T. Q. Cai, X. G. Li, Y. K. Wu, Y. W. Ma, Y. L. Ma, J. H. Wang, H. Y. Zhang, Y. P. Song, and L. M. Duan, Error analysis in suppression of unwanted qubit interactions for a parametric gate in a tunable superconducting circuit, Phys. Rev. A **102**, 022619 (2020).

[42] H. R. Lewis and W. B. Riesenfeld, An exact quantum theory of the time-dependent harmonic oscillator and of a charged particle in a time-dependent electromagnetic field, J. Math. Phys. **10**, 1458 (1969).

[43] X. Chen, E. Torrontegui, and J. G. Muga, Lewis-Riesenfeld invariants and transitionless quantum driving, Phys. Rev. A **83**, 062116 (2011).

[44] A. Ruschhaupt, X. Chen, D. Alonso, and J. G. Muga, Optimally robust shortcuts to population inversion in two-level quantum systems, New J. Phys. **14**, 093040 (2012).

[45] E. A. Sete, A. Q. Chen, R. Manenti, S. Kulshreshtha, and S. Poletto, Floating tunable coupler for scalable quantum computing architectures, Phys. Rev. Appl. **15**, 064063 (2021).

[46] F. Motzoi, J. M. Gambetta, P. Rebentrost, and F. K. Wilhelm, Simple pulses for elimination of leakage in weakly nonlinear qubits, Phys. Rev. Lett. **103**, 110501 (2009).

[47] J. M. Gambetta, F. Motzoi, S. T. Merkel, and F. K. Wilhelm, Analytic control methods for high-fidelity unitary operations in a weakly nonlinear oscillator, Phys. Rev. A **83**, 012308 (2011).

[48] T. Wang, Z. Zhang, L. Xiang, Z. Jia, P. Duan, W. Cai, Z. Gong, Z. Zong, M. Wu, J. Wu, L. Sun, Y. Yin, and G. Guo, The experimental realization of high-fidelity "shortcut-to-adiabaticity" quantum gates in a superconducting Xmon qubit, New J. Phys. **20**, 065003 (2018).

[49] J. Johansson, P. Nation, and F. Nori, QuTiP: An open-source python framework for the dynamics of open quantum systems, Comput. Phys. Commun. **183**, 1760 (2012).

[50] J. Johansson, P. Nation, and F. Nori, QuTiP 2: A python framework for the dynamics of open quantum systems, Comput. Phys. Commun. **184**, 1234 (2013).

[51] E. Knill, D. Leibfried, R. Reichle, J. Britton, R. B. Blakestad, J. D. Jost, C. Langer, R. Ozeri, S. Seidelin, and D. J. Wineland, Randomized benchmarking of quantum gates, Phys. Rev. A **77**, 012307 (2008).

[52] E. Magesan, J. M. Gambetta, and J. Emerson, Scalable and robust randomized benchmarking of quantum processes, Phys. Rev. Lett. **106**, 180504 (2011).

[53] E. Magesan, J. M. Gambetta, B. R. Johnson, C. A. Ryan, J. M. Chow, S. T. Merkel, M. P. da Silva, G. A. Keefe, M. B. Rothwell, T. A. Ohki, M. B. Ketchen, and M. Steffen, Efficient measurement of quantum gate error by interleaved randomized benchmarking, Phys. Rev. Lett. **109**, 080505 (2012).

[54] R. Barends *et al.*, Superconducting quantum circuits at the surface code threshold for fault tolerance, Nature **508**, 500 (2014).

[55] S. Filipp, P. Maurer, P. J. Leek, M. Baur, R. Bianchetti, J. M. Fink, M. Goppl, L. Steffen, J. M. Gambetta, A. Blais, and A. Wallraff, Two-qubit state tomography using a joint dispersive readout, Phys. Rev. Lett. **102**, 200402 (2009).

[56] J. M. Chow, L. DiCarlo, J. M. Gambetta, A. Nunnenkamp, L. S. Bishop, L. Frunzio, M. H. Devoret, S. M. Girvin, and R. J. Schoelkopf, Detecting highly entangled states with a joint qubit readout, Phys. Rev. A **81**, 062325 (2010).

[57] W. Zheng, J. Xu, Z. Ma, Y. Li, Y. Dong, Y. Zhang, X. Wang, G. Sun, P. Wu, J. Zhao, S. Li, D. Lan, X. Tan, and Y.

Yu, Measuring quantum geometric tensor of non-Abelian system in superconducting circuits, Chin. Phys. Lett. **39**, 100202 (2022).

[58] D. M. Abrams, N. Didier, B. R. Johnson, M. P. da Silva, and C. A. Ryan, Implementation of XY entangling gates with a single calibrated pulse, Nat. Electron. **3**, 744 (2020).

[59] S. A. Caldwell *et al.*, Parametrically activated entangling gates using transmon qubits, Phys. Rev. Appl. **10**, 034050 (2018).

[60] Q. Liu, Y. Guan, Y. Liu, H. Wang, Y. Li, Z. Ma, X. Tan, and R. Li, Phase calibration of the parametric gate in the superconducting circuits, Phys. Status Solidi B **260**, 2200474 (2022).